



Gold Recovery from E-Waste by Food-Waste Amyloid Aerogels

Journal Article

Author(s):

Peydayesh, Mohammad ; Boschi, Enrico; Donat, Felix ; Mezzenga, Raffaele

Publication date:

2024-05-09

Permanent link:

<https://doi.org/10.3929/ethz-b-000658267>

Rights / license:

[Creative Commons Attribution 4.0 International](#)

Originally published in:

Advanced Materials 36(19), <https://doi.org/10.1002/adma.202310642>

Gold Recovery from E-Waste by Food-Waste Amyloid Aerogels

Mohammad Peydayesh, Enrico Boschi, Felix Donat, and Raffaele Mezzenga*

Demand for gold recovery from e-waste grows steadily due to its pervasive use in the most diverse technical applications. Current methods of gold recovery are resource-intensive, necessitating the development of more efficient extraction materials. This study explores protein amyloid nanofibrils (AF) derived from whey, a dairy industry side-stream, as a novel adsorbent for gold recovery from e-waste. To do so, AF aerogels are prepared and assessed against gold adsorption capacity and selectivity over other metals present in waste electrical and electronic equipment (e-waste). The results demonstrate that AF aerogel has a remarkable gold adsorption capacity (166.7 mg g^{-1}) and selectivity, making it efficient and an adsorbent for gold recovery. Moreover, AF aerogels are efficient templates to convert gold ions into single crystalline flakes due to Au growth along the (111) plane. When used as templates to recover gold from e-waste solutions obtained by dissolving computer motherboards in suitable solvents, the process yields high-purity gold nuggets, constituted by $\approx 90.8 \text{ wt\%}$ gold (21–22 carats), with trace amounts of other metals. Life cycle assessment and techno-economic analysis of the process finally consolidate the potential of protein nanofibril aerogels from food side-streams as an environmentally friendly and economically viable approach for gold recovery from e-waste.

nanotechnology,^[5] medicine,^[6] and biotechnology.^[7] It has excellent conductivity, ductility, reflectivity, biocompatibility, and stability.^[8] For instance, its exceptional electrical conductivity makes it an integral component in the microelectronics industry; while, its catalytic prowess drives advancements in green chemistry and fuels innovations. As a non-renewable resource in high demand due to technological growth, recovering gold from waste sources such as municipal solid waste, e-waste, and industrial wastewater has become crucial, and in fact, an unavoidable strategy based on circular economy principles.^[8,9] E-waste is the fastest-growing global solid waste,^[10] with a production rate expected to reach 61.3 million tons in 2023.^[11] Gold is one of the most valuable components of e-waste, and its recovery can be highly profitable; yet, current adsorption methods using activated carbon are inefficient and resource-intensive,^[9,10] so that, the demand for more efficient materials to extract gold from e-waste has been on the continuous rise.^[12]

1. Introduction

Gold has been at the center of society development for millennia, at first for its precious and inert metal features, and more recently in human history, for its technical applications in electronics,^[1] catalysis,^[2] aerospace,^[3] electroplating,^[4]

The outstanding capability of protein amyloid fibrils (AF) as an adsorbent for removing heavy metals from water has been reported only recently, but since then, extensively documented and investigated.^[13] AF are novel nanofibril materials with distinct properties such as a high surface-to-volume ratio and highly modular surface functionality.^[14] They are made of repetitive core sequences with diameters ranging from 5 to 10 nm and lengths

M. Peydayesh, E. Boschi, R. Mezzenga
 Department of Health Sciences and Technology
 ETH Zurich
 Zurich 8092, Switzerland
 E-mail: raffaele.mezzenga@hest.ethz.ch

E. Boschi
 Laboratory for Cellulose & Wood Materials
 Empa-Swiss Federal Laboratories for Materials Science and Technology
 Dübendorf 8600, Switzerland

E. Boschi
 Department of Plant and Environmental Sciences
 University of Copenhagen
 Thorvaldsensvej 40, Frederiksberg C 1871, Denmark

F. Donat
 Department of Mechanical and Process Engineering
 ETH Zürich
 Leonhardstrasse 21, Zürich CH-8092, Switzerland

R. Mezzenga
 Department of Materials
 ETH Zurich
 Zurich 8093, Switzerland

 The ORCID identification number(s) for the author(s) of this article can be found under <https://doi.org/10.1002/adma.202310642>

© 2024 The Authors. Advanced Materials published by Wiley-VCH GmbH. This is an open access article under the terms of the [Creative Commons Attribution](https://creativecommons.org/licenses/by/4.0/) License, which permits use, distribution and reproduction in any medium, provided the original work is properly cited.

DOI: 10.1002/adma.202310642

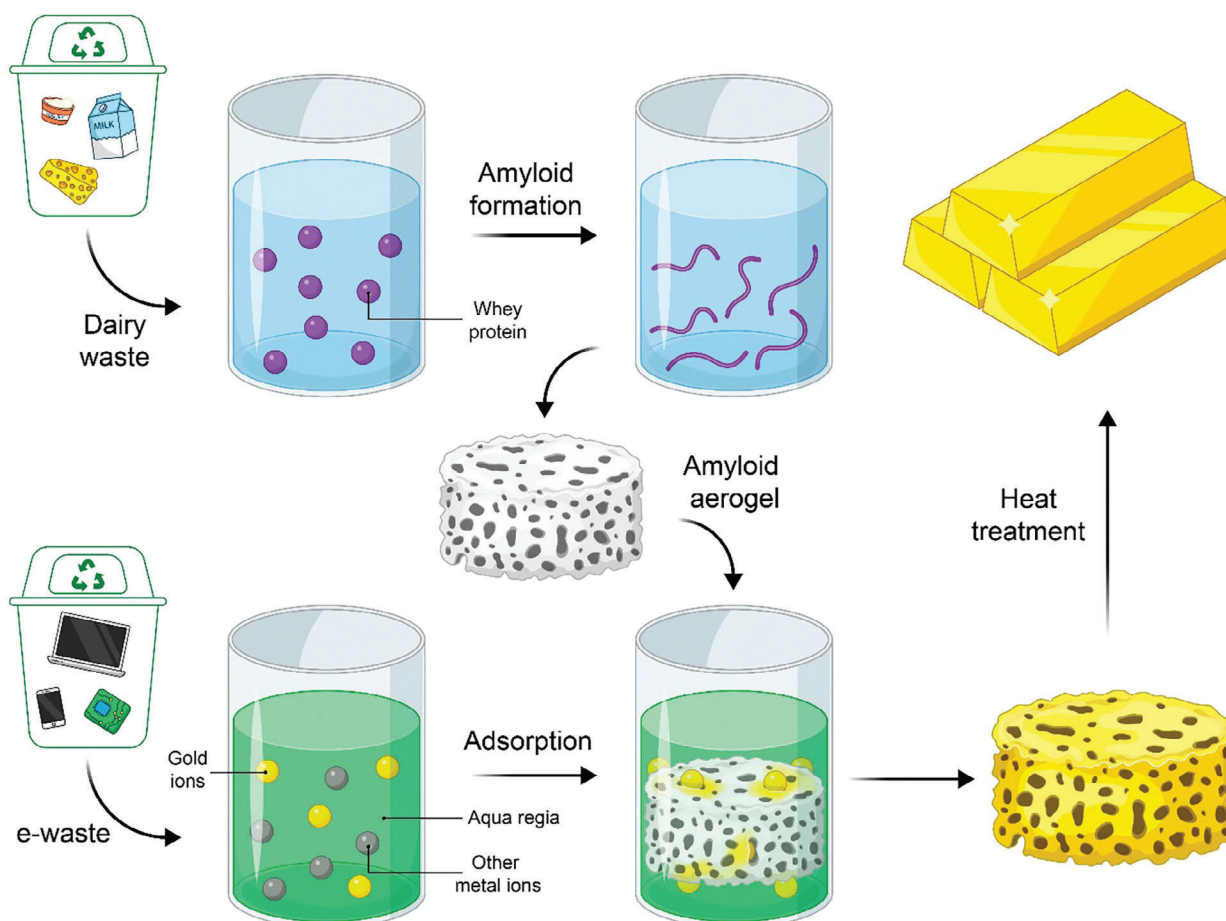


Figure 1. Schematic route followed to generate neat value via pure gold, extracted from food waste (whey) and e-waste as starting source materials.

ranging from one to several micrometers.^[15] AF are supramolecular polymers with a high concentration of β -sheet secondary structures held together by hydrogen bonds and van der Waals forces.^[16] They have exceptional nanomechanical properties, stability, distinct chirality, polarity, and charge characteristics.^[17] In recent years, AF have been investigated as scaffolds and building blocks for developing advanced materials for a multitude of applications.^[14,18] Interestingly, AF can also be produced from proteins extracted from food waste and industrial side streams.^[19] Food industry byproducts contain various proteins, such as whey, keratin, and plant proteins, which can readily form AF under specific conditions, facilitating the circularity and integrating these compounds into a new line of applications.^[20]

In this study, we show how whey, a major dairy industry side stream, can be valorized into AF aerogels for the selective recovery of gold from e-waste (Figure 1). In this win-win strategy, two major sources of waste, e-waste and food waste, are sustainably remediated, decreasing their environmental impacts and generating neat value from circular economy principles.

1.1. AF Aerogel

To start, AF were prepared by denaturation and self-assembly of whey protein at acidic conditions and high temperatures^[21] (re-

fer to the Experimental Section for details). The formation of a birefringent AF solution from whey was confirmed by a custom-made cross-polarizer device (Figure S1, Supporting Information). Atomic force microscopy (AFM) images of the AF, shown in Figure S2, Supporting Information reveal the emergence of elongated, linear, and semi-flexible fibrillar structures, each exhibiting a varied range of contour lengths spanning several micrometers. The whey AF aerogels were produced by freeze-drying the 2 wt% aqueous dispersion of AF and cross-linkers^[22] (see Experimental Section for details). As observed in Figure 2a, the resulting AF aerogels were light (a density of 33.18 mg cm^{-3} and a porosity of 97%) and featured excellent mechanical and water stability.

1.2. Metal Adsorption

The metal adsorption capacity of the ensued AF aerogels was assessed by measuring the concentration of the metals present in the solution before and after passive adsorption by the aerogel. The adsorption performance was calculated using Equations (1) and (2).

Figure 2b–d shows the aerogel performance in an equally distributed mixture of metals with known concentrations. As shown in Figure 2b, the gold concentration of the mixture decreased

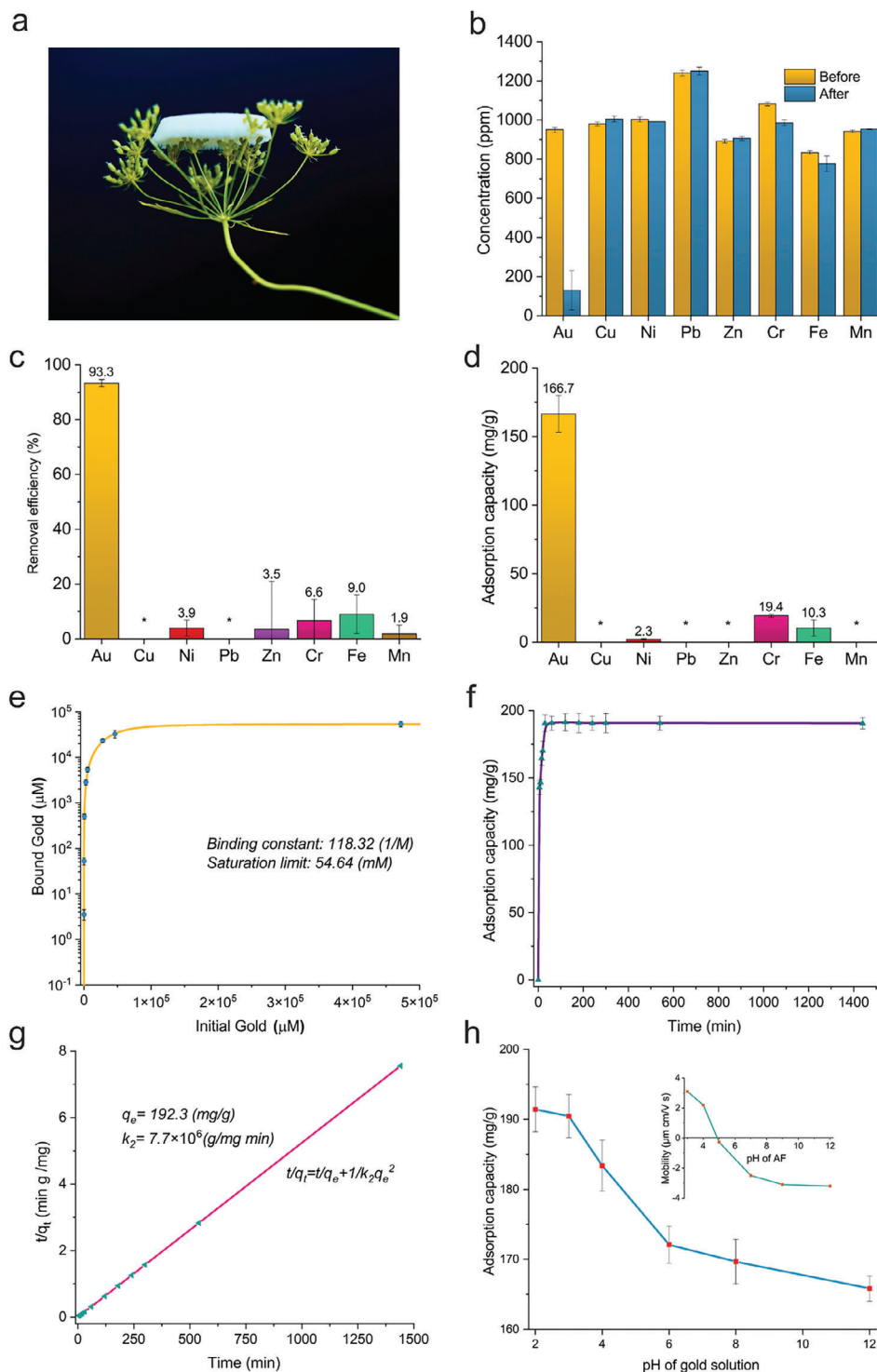


Figure 2. AF aerogels gold removing performance when used to treat a mixture of metals with approximately the same concentration. a) Photograph of a light AF aerogel on top of a flower. b) Concentration of the metals mixture before and after treatment with AF aerogel. c) Metals removal efficiency (%) of the AF aerogel in a mixture of metals with approximately the same concentration. d) Adsorption capacity of AF aerogel in a mixture of metals with approximately the same concentration. e) Fitted binding isotherms for gold (equilibrium concentrations vs initial concentrations). f) Gold adsorption capacity versus time at an initial concentration of 1000 ppm. g) The corresponding adsorption kinetics model fitting (pseudo-second-order). h) Effect of pH on gold adsorption by AF aerogel at an initial concentration of 1000 ppm (inset shows the electrophoretic mobility of AF at different pH values). (*) indicates zero values.

from 950 to 130 ppm after treatment with the AF aerogel. This suggests that the AF aerogel adsorbed 3320 μg of gold. Further, Figure 2b shows that the other concentrations changed only marginally, if at all, apart from gold. This can be further underlined by the characteristic parameters of the aerogel performance, shown in Figure 2c,d. As observed, the aerogels had a removal efficiency of 93.3% for gold and an adsorption capacity of 166.7 mg g^{-1} . In contrast, for Cu, Ni, Pb, Zn, Cr, Fe, and Mn, the removal efficiencies were 0%, 3.9%, 0%, 3.5%, 6.6%, 9%, and 1.9%, respectively (Figure 2c). The adsorption capacities for Cu, Ni, Pb, Zn, Cr, Fe, and Mn were 0, 2.3, 0, 0, 19.4, 10.3, and 0 mg g^{-1} , respectively (Figure 2d). These results—which, as it should be noted are acquired in conditions of passive adsorption from extremely highly concentrated heavy metal solutions—demonstrate the excellent selectivity of the AF aerogels for gold ions compared to other metal ions. The primary mechanism driving metal removal by AF aerogel involves supramolecular chemical chelation between various amino acids present on the AF surface and metals. This process entails the formation of multiple coordination bonds between protein organic molecules and a central metal atom, ultimately leading to the sequestration of the metal. Notably, amino acids such as cysteine, aspartic acid, glutamic acid, and histidine emerge as the most favorable motifs for coordinating heavy metals. The previous observations showed a correlation between metal–protein chelation bond strength and the molecular weight of the metals.^[13a,14] Heavier metals exhibit stronger bonds, which confirms the high affinity of AF aerogels toward gold. However, chelation alone does not account for the complete mechanism of pollutant removal by protein nanofibrils. Local electrostatic and hydrophobic interactions induced by the polyampholytes AF, along with hydrogen bonding, also play important roles in the binding process.^[14] Among the metals scrutinized in this study, gold only exists in an anionic form (AuCl_4^-), which enhances its absorption on positively charged AF aerogels based on electrostatic interactions. Moreover, the effect of metals' valency and their counterions on these interactions should not be overlooked. It is noteworthy that in adsorption events involving various metals, the kinetics of adsorption must be considered. In our investigation, gold demonstrated a faster adsorption rate by the aerogel, occupying all active sites. This efficient adsorption of gold hindered the effective adsorption of other heavy metals such as Pb and Ni by AF aerogels. A possible mechanism for the adsorption of gold ions onto the AF aerogel can be postulated based on previous work:^[9] In an acidic environment, AuCl_4^- was electrostatically adsorbed onto the protonated positive groups of the AF aerogel. Subsequently, amino acids such as Tryptophan, Histidine, Tyrosine, and Aspartic acid reduced Au^{3+} to metallic gold (Au^0). Finally, the formed nanoparticles were rapidly stabilized via the development of Au–S bonds between Au^0 and cysteine residues, owing to the robust coordination between gold and thiol groups.^[9]

To elucidate further on the adsorption of gold by AF aerogel, we studied the adsorption isotherm and kinetics and the effect of pH. First, we assessed the adsorption equilibrium, binding constant, and maximum adsorption capacities of gold on AF aerogels across a range of concentrations from 1 to 100 000 ppm (Figure 2e; Figure S3, Supporting Information). The isotherm, depicted in Figure 2e, using the Swillens and Motulsk approach,^[23] exhibited an L-curve pattern, underscoring that as

the gold concentration increases, locating vacant binding sites becomes progressively challenging.^[24] The saturation limit and binding constant were determined as 54.64 mm and 118.32 M^{-1} , respectively. Notably, the maximum adsorption capacity of AF aerogels for gold increased from 0.12 mg g^{-1} at an initial gold concentration of 1 ppm to an impressive 1887 mg g^{-1} at an initial gold concentration of 100 000 ppm. At 1000 ppm, the gold adsorption capacity reached 190 mg g^{-1} , slightly surpassing the capacity in a mixed-metal environment with the same concentration.

Moving on to the kinetics of gold adsorption on AF aerogel, we tracked the reduction in gold concentration over various time intervals (Figure 2f). Within a mere 5 min of contact with AF aerogel, the gold concentration decreased by 77%, corresponding to an adsorption capacity of 143 mg g^{-1} , and reached a plateau after 30 min. This sudden decline implies a rapid mass transfer of gold ions and their prompt interaction with the binding sites of AF aerogels. Figure 2g demonstrates that this rapid adsorption process adheres to a pseudo-second-order reaction, indicating chemisorption as the primary mechanism of adsorption reactions.^[25]

Finally, we explored the effect of gold solution pH on adsorption capacity at an initial concentration of 1000 ppm and pH values of 2, 3, 4, 6, 8, and 12. As depicted in Figure 2h, an increase in pH led to a continuous decrease in adsorption capacity. AF possesses an isoelectric point around 5, rendering them positively charged at pH values below 5 and negatively charged at pH values above 5 (refer to the inset of Figure 2h). Elevating the pH results in a decrease in the electrophoretic mobility of AF, shifting toward negative values.^[26] These findings underscore the impact of electrostatic interactions in total binding events, where HAuCl_4^- anions are adsorbed by the positively charged surface of AF aerogels in acidic conditions, leading to higher adsorption capacities. Nevertheless, the difference in adsorption capacities between pH 2 and pH 12 is only 15%, indicating that the adsorption phenomena are supramolecular events involving more than mere electrostatic interactions.

AF are not only able to remove gold ions efficiently but also can convert these ions into gold nanoparticles and elemental single crystalline flakes. Figure 3a shows the formation of gold nanoparticles (purple-colored parts) on the surface of the AF aerogel during the treatment of a low-concentrated gold solution (10 ppm).^[27] Moreover, when the concentration of the gold solution was increased to 1000 ppm, the AF aerogel not only adsorbed gold but also reduced it to its single crystalline form (Figure 3b). This was supported by the light microscopy images from the AF aerogel sample shown in Figure 3c.^[28] A distinct visual confirmation of the gold microplates formation on the interior surfaces of the AF aerogel is provided by scanning electron microscopy (SEM) (Figure 3d). As observed, the microplates maintained triangular and hexagonal shapes of various sizes, but always, with 120° angular symmetry. The observed variation in size and the nature of the produced gold (nanoparticles and nanosheets) can be ascribed to the intricate interplay of amino acids, which influence both the reduction and capping effects, along with the concentration of gold. Amino acids exhibiting slower reduction rates and stronger capping effects, characterized by attachment on two planes of particles and influencing crystal growth from the sides, were identified as promoting the 2D growth of gold crystals

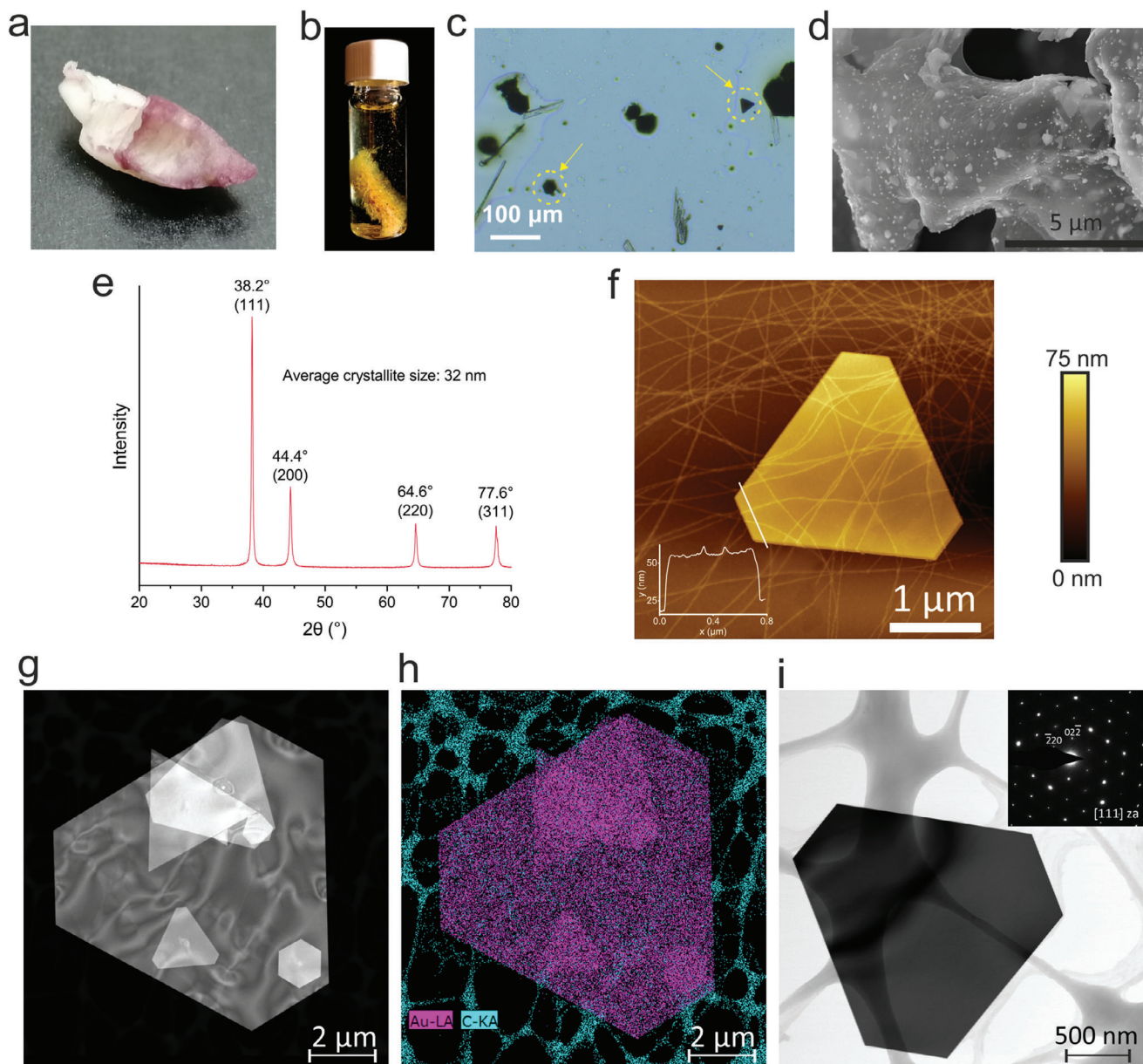


Figure 3. Gold nanoparticles and crystal formation using AF aerogels. a) Formation of gold nanoparticles on the surface of AF aerogel after adsorption of a 10 ppm gold metal mixture. b) Gold crystal formation on AF aerogel in a 4 mL glass vial containing the 1000 ppm metal mixture. c) Optical microscopy images taken from a sample of the AF aerogel shown in (b). d) SEM image of an AF aerogel loaded with newly formed gold crystals. e) XRD pattern of gold nanoplates obtained by the adsorption and reduction of Au³⁺ by AF aerogel. f) AFM of gold hexagonal microplates formed by AF (the inset shows the height distribution along the profile line). g) The HAADF-STEM image. h) The color map of the EDS spectrum image of the particle in (g) shows the color overlay of Au-L α and C-K α signals. i) The BF STEM micrograph of an Au-platelet and the corresponding SAD pattern acquired from the particle in the electron diffraction mode. The SAD pattern reveals the [111] plane orientation of the particle platelet.

through a kinetically controlled synthesis pathway.^[29] For lower concentrations of gold ions, the reduction process tended to favor the formation of smaller entities, specifically gold nanoparticles. This prevailing behavior toward smaller structures was attributed to the limited concentration of gold ions available to support the formation of larger entities, or equivalently, an increased protein/ions ratio favoring heterogeneous nucleation over growth. The fine balance between nucleation and growth, in combination with the capping behavior of the AFs, led to

the intriguing transformation of gold nanoparticles into gold nanosheets.^[30]

Powder X-ray diffraction (XRD) analysis was employed to validate the crystalline nature of the gold nanoplates formed on the AF aerogels (Figure 3e). The presence of four distinct peaks at 2θ angles of 38.2°, 44.4°, 64.6°, and 77.6° can be associated with the characteristic Bragg reflections corresponding to the (111), (200), (220), and (311) crystallographic planes of the face-centered cubic (fcc) lattice structure of elemental gold metal (Au⁰),

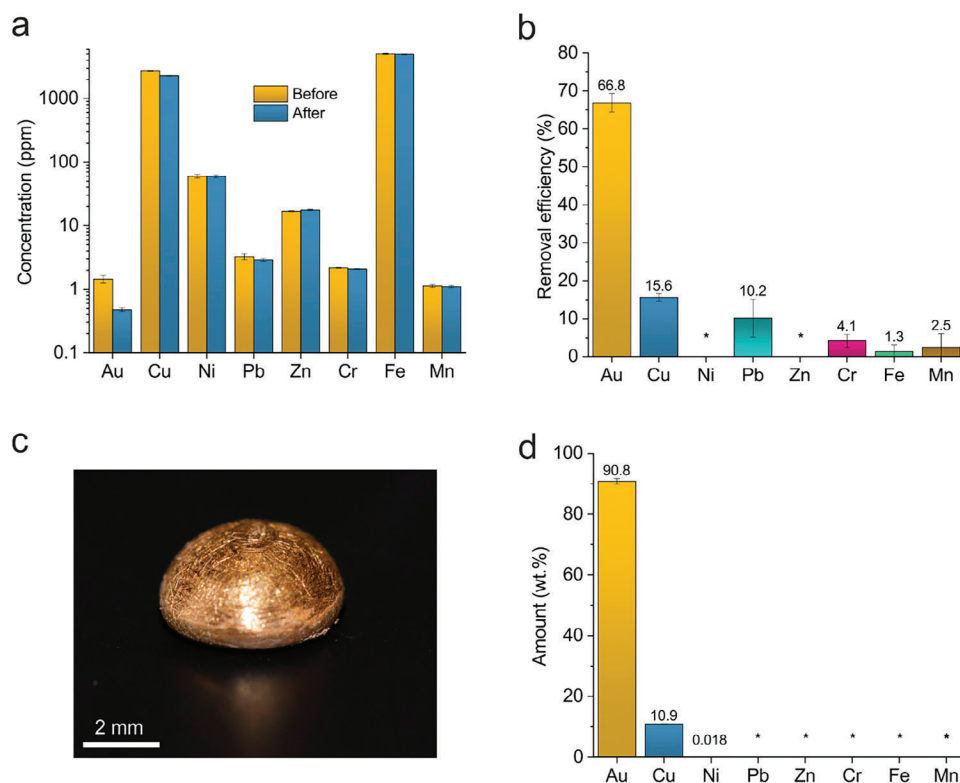


Figure 4. AF aerogel performance to treat and recover gold from e-waste solutions. a) Metal concentration before and after AF aerogel treatment. The concentration is plotted using a logarithmic scale to highlight the differences in composition among the various heavy metals. b) Removal efficiency of the AF aerogel (* values are zero). c) Photograph of the recovered gold nugget from e-waste. d) Metal composition of the recovered nugget obtained by ICP-OES (* values are below 0.025 wt%).

confirming the formation of crystalline gold nanoplates.^[31] Using the Scherrer equation, the average crystallite size was determined to be 32 nm. Figure 3f shows a high magnification AFM image of gold single crystals microplates formed by the reduction in the presence of AF. The corresponding topographic height analysis shows that the polygonal single crystal appears perfectly flat and maintains a consistent height of ≈ 55 nm. Figure 3g–i presents the scanning transmission electron microscopy (STEM) analyses of the gold platelets, the formation of which was facilitated by AF. Figure 3g, the high-angle annular dark field (HAADF) image, clearly demonstrates the prominently polygonic morphology of the faceted particles found all over the transmission electron microscopy (TEM) samples. As the HAADF imaging is an atomic number sensitive mode, the high atomic number of Au is responsible for the bright against black background contrast in the micrograph. The elemental content of the particles was verified by the energy dispersive X-ray spectroscopy (EDS) STEM analyses employed in the drift-corrected Spectrum Imaging (SI) mode of EDS STEM. Figure 3h shows the color overlay of Au–L_a and C–K_a signals of the particle in Figure 3g and confirms that the observed polygons of very regular shape are Au-platelets (purple) lying on the lacy amorphous carbon foil (cyan) of a TEM support grid. The Au-platelets are virtually 2D; and therefore, an enhanced Au–L_a signal in the particle overlap regions. The bright field (BF) STEM micrograph in Figure 3i shows one of the particles and the corresponding selected area diffraction (SAD) pattern acquired in a TEM operation mode from the

same particle. The SAD represents very thin flakes with the very characteristic feature of the platelets, the most prominent [111] out-of-plane crystallographic orientation of the platelets. These results are consistent with a 2D growth of the Au crystals propagating on the (111) plane, presumably promoted by the inhibition of growth on the [111] direction by the planar adsorption of amyloid fibrils on the 2D surface of the growing Au single crystal.^[32]

1.3. Recovery of Gold from E-Waste

Having established the high Au adsorption capacity and selectivity of the AF aerogels, these were then used for gold recovery from a solution produced by dissolving the computer motherboards in aqua regia, as described in the Experimental Section. As illustrated in Figure S4, Supporting Information, the AF aerogel remained stable, retaining its shape and structure, even after being immersed in aqua regia. Notably, as AF are prepared in an HCl acidic solution with a pH of 2, their exposure to acidic conditions, such as aqua regia, caused no change in their fibrillar structures, and only mild aggregation was observed (Figure S5, Supporting Information). As shown in Figure 4, the concentration of gold in the solution before treatment with the AF was 1.44 ppm, much lower than other metals such as copper (2711 ppm) or iron (5033 ppm). Yet, the AF aerogels featured a remarkable adsorption capability even in these conditions, decreasing the gold content of the solution after treatment

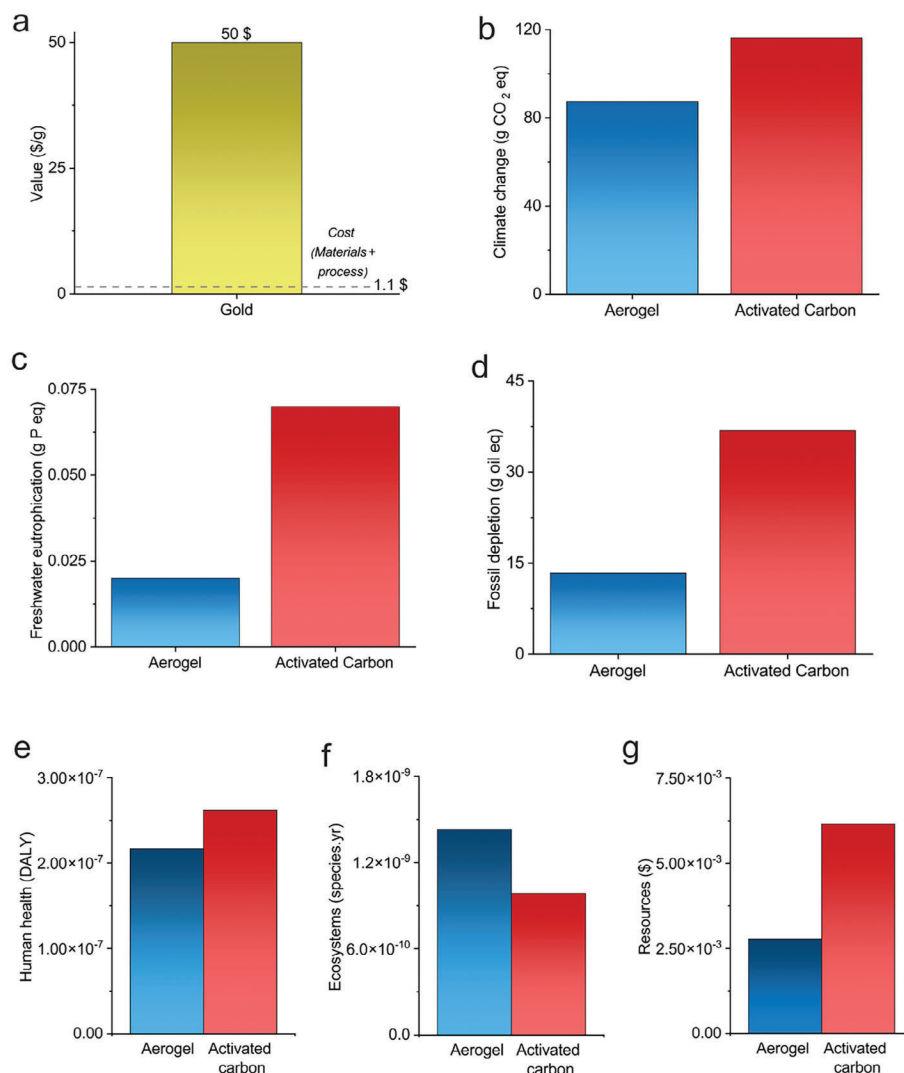


Figure 5. Techno-economic analysis and LCA of gold recovery from e-waste by AF Aerogels. a) Summary of techno-economic analysis. Midpoint environmental impacts: b) climate change, c) freshwater eutrophication, and d) fossil depletion. Endpoint damage assessment results: e) human health, f) ecosystems, and g) resources.

to 0.48 ppm (Figure 4a). As observed in Figure 4b, this reduction in gold concentration was equal to a removal efficiency of 66.8%; while, the removal efficiency for copper (the second most adsorbed metal) was only 15.6%, indicating, once again, the high gold selectivity of AF aerogels. The variations in adsorbent removal efficiency between the solution of metals prepared by dissolving equal amounts of specific metal salts in water and the extracted metal solutions from e-waste, can be attributed to several factors. First, the dissimilarity in metal concentrations in the two solutions plays a crucial role. In the case of the synthetic mixture, metals are present in predetermined and uniform concentrations, whereas in e-waste solutions, the concentrations can vary significantly. In addition, differences in the ionic types, valences, and counterions of metals contribute to the observed variations in removal efficiency. The synthetic mixture involves metals in specific ionic forms, whereas e-waste solutions may contain metals with diverse ionic characteristics and valency states. Further,

the counterions accompanying the metals in each solution differ, adding another layer of complexity. Last, the presence of other solutes in e-waste solutions has a notable impact on adsorption capacities. These additional substances, whether organic or inorganic, can compete with the target metals for adsorption sites, potentially hindering the overall effectiveness of the adsorption process.

As depicted in Figure 5a, after adsorbing the gold ions, the AF aerogels were subjected to thermal treatment, and eventually, a gold nugget was recovered from this process with a mass of 0.5 g. To ascertain the precise metal composition of the recovered nugget, ICP-OES was employed. Figure 5b presents each metal's amount, that is, Au, Cu, Fe, Pb, Ni, Zn, Cr, and Mn, in the recovered nugget. The analysis revealed that the nugget predominantly contains gold (90.8 wt%), with copper and nickel contributing 10.9 wt% and 0.018 wt%, respectively. The remaining detected metals were found in trace amounts below

0.025 wt%. These findings demonstrate the high purity of the retrieved gold nugget, corresponding to ≈ 21 – 22 carats.

To establish the economic viability of recovering gold from e-waste using AF aerogel and to underscore its potential for scalability, a simplified techno-economic assessment was conducted using the data inventory detailed in Table S1, Supporting Information. The result shown in Figure 5a reveals that the total cost associated with recovering 1 g of gold from e-waste using AF aerogel, encompassing both material and process expenses, amounts to 1.1\$. Given the prevailing market value of ≈ 50 \$ per g for 22-carat gold, these findings emphasize the economic advantage of recovering gold from e-waste using AF aerogel.

To elucidate the environmental impacts of gold adsorption from e-waste using AF aerogel, we conducted an in-depth LCA analysis. A comparative assessment was performed comparing the outcomes with those obtained from activated carbon, a conventional adsorbent employed in gold recovery processes. The LCA functional unit was the recovery of 1 g of gold from e-waste. The respective gold adsorption capacities of AF aerogel and activated carbon were 190 and 66 mg g⁻¹. Consequently, to achieve the LCA objective of recovering 1 g of gold from e-waste, 5.26 and 15.15 g of AF aerogel and activated carbon were needed, respectively. Comprehensive life cycle inventory (LCI) data for both adsorbents are presented and summarized in Table S2, Supporting Information. The LCA outcomes of the most pertinent midpoint impacts and endpoint damages are consolidated within Tables S3 and S4, Supporting Information; Figure 5b–g. As depicted in Figure 5b, the carbon footprint of using AF aerogel in gold recovery approximates 87 g CO₂ equiv., whereas this quantity reaches 116 g CO₂ equiv., for activated carbon deployment. Compared to activated carbon, using AF aerogel as an adsorbent for gold recovery results in a 71% decrease in freshwater eutrophication and a 64% decrease in fossil depletion (Figure 5c,d). A more comprehensive assessment is extended to the three endpoint damages encompassing human health, ecosystems, and resources (Figure 5e–g). As observed in Figure 5e,g, AF aerogels consistently exhibit lower damage across human health and resources than activated carbon. The main reason for the higher environmental impact of using activated carbon compared to AF aerogel is its higher energy consumption during production (predominantly derived from non-renewable fossil sources),^[33] coupled with the greater amount of adsorbent requisite due to its lower adsorption capacity compared to AF aerogel. However, AF aerogels show more damage to ecosystems compared to activated carbon (Figure 5f). The LCA analysis reveals that most of this damage originates from using whey protein. One approach to mitigate and lower ecosystem damage is the transition from animal-based proteins to plant-based proteins. Indeed, our LCA analysis shows that by changing the protein type from whey to pea and potato proteins, the ecosystem damage decreased by 41% and 53%, respectively, and was placed below the ecosystem damage of activated carbon. Altogether, these results underscore the economic viability and environmental superiority of AF aerogels in the context of gold recovery from e-waste.

2. Conclusion

In this study, we demonstrated the successful use of AF aerogels derived from food side-streams, for example, whey pro-

tein, as an efficient and selective adsorbent for gold recovery from E-waste. The AF aerogels exhibited remarkable gold adsorption capacity and selectivity over other metals present in E-waste, making them a promising material for sustainable gold extraction. In addition, the AF aerogels were able to convert gold ions into gold nanoparticles and elemental crystalline flakes during the adsorption process. The AF aerogels were employed to recover gold from E-waste solutions obtained by dissolving computer motherboards, resulting in a high-purity gold nugget of ≈ 21 – 22 carats. These findings, along with life cycle assessment and techno-economic analyses of the process, run with realistic benchmarks, demonstrate the potential of AF aerogels as a novel environmentally friendly approach to address the growing demand for gold recovery from E-waste, contributing to circular economy principles and sustainable resource management.

3. Experimental Section

Materials: Whey protein isolate was provided from Fonterra and directly used for AF preparation. Hydrochloric acid (HCl, 37%), Nitric acid (HNO₃, 65%), sodium borate, sodium hypophosphite (SHP), and 1,2,3,4 butanetetracarboxylic acid (BTCA) were purchased from Sigma Aldrich.

For the preparation of the standard metal solutions, the following metal salts were used: Pb(NO₃)₂, Cu(NO₃)₂, H₂AuCl₄, CrO₃, Ni(NO₃)₂, MnCl₂, FeCl₃, ZnCl₂. All metal salts were provided by Sigma Aldrich. A piece of Britta filter (around 100 mg) made from activated carbon from coconuts shells was used to compare gold adsorption performance.

The computer motherboards (ASUS P5KPL AM, HP, and DELL) were purchased from Ruhoff-Informatik GmbH Pfannestiel 12A, 4624 Härkingen SO. They were prepared and disassembled using a wrench, flat-nose pliers, hammers, screwdrivers, and working gloves.

Methods: AF Preparation: To prepare AF, first, a 2 wt% whey solution was made using 10 g whey protein powder and 490 mL Milli-Q water. Then, the pH of the solution was adjusted to 2 using 1 M HCl solution. After that, the solution was incubated at 90 °C for 5 h (Figure S1, Supporting Information). Then, the protein solution was cooled down by quenching into an ice bath. Finally, the bottle was put into polarized light to check for birefringence and to determine if AF formed.

Aerogel Production: To produce the cross-linked AF aerogel, BTCA as the crosslinker and SHP as the catalyst were used (Figure S1, Supporting Information). BTCA was added at an AF to BTCA weight ratio of 1:0.2. SHP, on the other hand, was added at an SHP to BTCA weight ratio of 2:1.^[22] Then, the homogenous mixture was poured into a 3 mL aluminum mold. The molds containing the mixture were stored at -20 °C and subsequently freeze-dried. The cross-linking was achieved by putting the as-prepared aerogels into an oven for 15 min at a temperature of 175 °C.

Pure Metal Adsorption: To systematically assess the removal performance of the aerogel for each heavy metal, a solution of nine metal ions (Au, Cu, Ni, Zn, Pb, Fe, Mn, and Cr) was produced. The concentration of the pure metal solutions was adjusted to 10 and 1000 ppm. To evaluate the adsorption performance, a piece of aerogel (around 100 mg) was added to 20 mL of heavy metals solution. After adding the aerogel, all vials were stored at room temperature for 24 h. All aerogel samples were analyzed in triplicates to determine the total metal content. To do so, an AA240FS fast sequential atomic absorption spectrometer (flame AAS) from Varian was used. Then, the adsorption capacity (q) and removal efficiency (R) were calculated by Equations (1) and (2), respectively, as follows:

$$q \left[\frac{\text{mg}}{\text{g}} \right] = \frac{C_{\text{before}} \left[\frac{\text{mg}}{\text{L}} \right] - C_{\text{after}} \left[\frac{\text{mg}}{\text{L}} \right]}{m \left[\text{g} \right]} \times V \left[\text{L} \right] \quad (1)$$

$$R [\%] = \frac{C_{\text{before}} \left[\frac{\text{mg}}{\text{L}} \right] - C_{\text{after}} \left[\frac{\text{mg}}{\text{L}} \right]}{C_{\text{before}} \left[\frac{\text{mg}}{\text{L}} \right]} \times 100 \quad (2)$$

where C and m stand for the concentration of metal ions and the mass of aerogel, respectively.

Gold Adsorption Studies: For binding isotherms, pure gold solutions ranging from 1 to 100 000 ppm were prepared. To investigate adsorption equilibrium, these solutions were then exposed to a constant amount of aerogel for 24 h. To fit the binding isotherms, Equation (3) was employed. This equation assumes a single binding gold-ligand pair with a singular average binding constant.^[23] In this approach, $[P]$ and $[L]$ represent the concentrations of bound gold and ligand, respectively. In addition, $[P_0]$ and $[L_0]$ denote the initial total concentrations of gold and ligand; while K_a represents the binding constant.

$$[P \times L] = \frac{1}{2} \left([P_0] + [L_0] + \frac{1}{K_a} \right) - \frac{1}{2} \sqrt{\left([P_0] + [L_0] + \frac{1}{K_a} \right)^2 - 4 [P_0] [L_0]} \quad (3)$$

The kinetic experiments were performed at a gold concentration of 1000 ppm. Pseudo-second order kinetic model^[34] was applied to fit the experimental data of gold adsorption onto amyloid fibril aerogel:

$$\frac{t}{q_t} = \frac{1}{k_2 q_e^2} + \frac{1}{q_e} \times t \quad (4)$$

where t , k_2 , q_t , and q_e are adsorption time (min), rate constant of second-order sorption (g/min mg), and gold uptake capacities at any time t and at equilibrium (mg g⁻¹), respectively. The constants, k_2 and q_e can be determined by plotting t/q_t as a function of time.

To determine the effect of pH, aerogel was put in a gold solution with concentration of 1000 ppm, and then, the pH was adjusted to 2, 3, 4, 6, 8, and 12 using 1 M HCl and 1 M NaOH.

Gold Recovery from E-Waste: Figure S6, Supporting Information shows the steps for gold recovery from motherboards using AF aerogels. First, all plastic encasings were removed from the motherboard. In addition, all metal encasing from the ports, slots, and connections was pulled off. After that, all capacitors and inductors were detached. Next, the processor was removed, and the processor casing was dismantled. The CPU socket was taken out as well. All plastic and metal encasing, the capacitors, the inductors, and the processor encasing were trashed. After all removable parts were taken off, the remaining motherboard parts were smashed into pieces with a length of ≈ 5 cm and a width of ≈ 4 cm. The produced motherboard pieces were collected and put together with the CPU. Aqua regia (molar ratio HCl:HNO₃ = 3:1) was used to dissolve and extract the metals from the collected motherboard parts and the CPU. The ratio of the motherboard parts weight to aqua regia volume was set to 0.815.^[9] After the needed aqua regia volume was known, it was prepared in a glass beaker to hold the respective volume. As soon as the aqua regia was ready, the motherboard parts were added to the glass beaker. This extraction step was performed with the ventilation set to maximum as the reaction was very strong. After 24 h of reaction, the motherboard parts and the CPU were fully dissolved, and the resulting solution was filtered using a 0.45 μm filter paper. Eventually, the second filtration was performed using a 0.22 μm syringe membrane. To recover gold, first, a 1200 mL plastic beaker was filled with the filtrated solutions. Thereafter, 30 aerogels (mg each) were added. The beaker was placed on a magnetic stirrer and kept in a fume hood at room temperature for 24 h. Afterward, the aerogels were collected and dried at 60 °C for 24 h. The dried aerogels were then combusted in the air in a muffle furnace (Heraeus Instruments, Type M110) in two steps at 500 °C for 1 h, and then, at 1000 °C for 2 h. Next, the combustion product (ash and adsorbed metals) was mixed with sodium borate (borax) powder. The mixture of borax and ash was transferred into an alumina crucible and melted using an acetylene torch. The gold clump was retrieved from the crucible as soon as the crucible and the melted gold cooled down.

Gold Crystals Characterization: An upright microscope (Zeiss Axiolmager.Z2) with a 10 \times objective was used to obtain the optical microscopy image of the gold microplates. The formation of gold microplates in the inner structure of AF aerogel was characterized using a Hitachi SU5000 scanning electron microscope (SEM). Prior to capturing SEM images, small pieces of the aerogels were coated with a 5 nm layer of platinum/palladium; while, being rotated on a planetary system (Safematic, CCU-10, Switzerland). The XRD pattern of the gold nanoplates loaded AF aerogel was measured with a PANalytical Empyrean X-ray diffractometer. The instrument was equipped with an X'Celerator Scientific ultra-fast line detector and Bragg-Brentano HD incident beam optics using Cu K α radiation ($\lambda = 1.5418 \text{ \AA}$, 45 kV and 40 mA). The measurement was conducted in the 2θ range 10–90° with a step size of 0.0167°, and the total measurement time was 30 min. The atomic force microscopy (AFM) measurements were done on a Bruker Icon3 AFM. First, the gold and whey protein amyloid solutions were pipetted onto a freshly prepared mica sheet and incubated for 1 min. Afterward, the samples were rinsed with Milli-Q water and dried with air. For all the measurements, RTESPA-150 tips for tapping in soft tapping mode were used. The vibration frequency was 150 kHz. The AFM images were processed with Gwyddion. First, the image was leveled by subtracting the mean level value of the image, and then, polynomial corrections were applied to the background. Further, the scale was corrected by putting the minimal values of the image to zero. Last, the height data were extracted by measuring the height difference over the line which crosses the gold plate. Morphological and analytical characterization of the material on the nanoscale was performed in the work by TEM on a TFS Talos F200X instrument operated at 200 kV acceleration voltage in both TEM and STEM operating modes. The TEM mode was primarily employed for the electron diffraction analyses of the crystalline Au-nanoparticles using the SAD analyses from ≈ 900 nm in diameter areas of the Au-particles. The whole body of the microstructure studies was carried out by STEM using a probe size of ≈ 0.25 nm (convergence angle 10.5 mrad) and coaxially positioned annular dark field and circular bright field detectors. The simultaneous acquisition of the scattered signals by coaxial detectors enabled the collection of complementary information from the same volume of the material. The collection angles of two annular detectors were set so that the HAADF, 70–120 mrad, produced prominent atomic number contrast from different atomic species of the material, whereas the low-angle annular dark field detector (LAADF), 15–68 mrad, also provided a clear diffraction contrast from crystalline volumes in the illumination specimen region. Moreover, the circular BF STEM detector, positioned precisely on the optical axis, complemented the information by giving the signal within 11 mrad of the collection angle. The EDS employed in the STEM mode provided the analytical information from the material region. The EDS STEM studies were carried out using the SuperX EDS module of Talos, consisting of four symmetrically positioned above the specimen EDX detectors. The SI mode of the EDX signals acquisition provided the drift-corrected elemental content distribution maps. The L-series of Au and K-series of the rest of the elements' emission spectra were used for the elemental maps and their overlays.

Determination of Different Metal Amounts in the Recovered Nugget: To determine the amount of Au, Cu, Fe, Pb, Ni, Zn, Cr, and Mn in the recovered metal nugget, inductively coupled plasma optical emission spectroscopy (ICP-OES) was used (PlasmaQuant PQ Elite, Analytik Jena). To do so, ≈ 0.1 g of the sample was weighted. A mixture of HCl/HNO₃ was added, and samples were heated in a heating block at 90 °C. After dissolution, samples were completed to 50 mL with Milli-Q water. Three independent tests were performed for each sample.

LCA Study: The LCA assessment was conducted in accordance with the ISO 14040/44 standard protocol, adopting an attributional and prospective approach for an emerging product, aligning with the methodologies employed in studies by Walser et al.^[35] and Arvidsson et al.^[36] This investigation focused on comparing the environmental impacts of employing AF aerogels and activated carbon in a static adsorption process for the recovery of 1 g of gold from a pure gold solution with a concentration of 1000 ppm. The LCA specifically evaluated the cradle-to-use life cycle impacts of the adsorbents. A life cycle inventory (LCI) for the two adsorbents was conducted and is succinctly presented in Table S2, Supporting

Information. Process data for AF aerogel were directly derived from the authors' laboratory experiments; while, inventory data for all input materials and energy sources were obtained from the Ecoinvent 3 database. Life cycle models were constructed using SimaPro v. 9.3.0.3. To assess the impact of the LCI, the ReCiPe midpoint and endpoint methods were employed to cover a broad spectrum of impact categories.

Supporting Information

Supporting Information is available from the Wiley Online Library or from the author.

Acknowledgements

The authors thank C. Zeder for assisting with the atomic absorption spectrometry, Eurofins EAG Laboratories for performing inductively coupled plasma optical emission spectroscopy, and Y. Yuan from ETH Zurich for optical microscopy. The authors gratefully acknowledge the support of A. Sologubenko from the Scientific Center of Optical and Electron Microscopy of ETH Zurich (ScopeM) for scanning transmission electron microscopy.

Open access funding provided by Eidgenössische Technische Hochschule Zurich.

Conflict of Interest

The authors declare no conflict of interest.

Data Availability Statement

The data that support the findings of this study are available from the corresponding author upon reasonable request.

Keywords

aerogel, e-waste, food waste, gold recovery, life cycle assessment, protein nanofibrils

Received: October 12, 2023
Revised: November 30, 2023
Published online: January 29, 2024

- [1] P. Goodman, *Gold Bull.* **2002**, *35*, 21.
- [2] D. T. Thompson, *Nano Today* **2007**, *2*, 40.
- [3] M. Aamir, K. Giasin, M. Tolouei-Rad, A. Vafadar, *J. Mater. Res. Technol.* **2020**, *9*, 12484.
- [4] B. Satpathy, S. Jena, S. Das, K. Das, *Int. Mater. Rev.* **2022**, *68*, 825.
- [5] I. Hammami, N. M. Alabdallah, *J. King Saud Univ., Sci.* **2021**, *33*, 101560.
- [6] M. Yadid, R. Feiner, T. Dvir, *Nano Lett.* **2019**, *19*, 2198.
- [7] D. Lin, Z. Qian, M. Bagnani, M. A. Hernández-Rodríguez, J. Corredoira-Vázquez, G. Wei, L. D. Carlos, R. Mezzenga, *ACS Nano* **2023**, *17*, 9429.
- [8] T. Ma, R. Zhao, Z. Li, X. Jing, M. Faheem, J. Song, Y. Tian, X. Lv, Q. Shu, G. Zhu, *ACS Appl. Mater. Interfaces* **2020**, *12*, 30474.
- [9] F. Yang, Z. Yan, J. Zhao, S. Miao, D. Wang, P. Yang, *J. Mater. Chem. A* **2020**, *8*, 3438.
- [10] F. Li, J. Zhu, P. Sun, M. Zhang, Z. Li, D. Xu, X. Gong, X. Zou, A. K. Geim, Y. Su, H.-M. Cheng, *Nat. Commun.* **2022**, *13*, 4472.
- [11] G. Wójcik, M. Górska-Parat, Z. Hubicki, K. Zinkowska, *Materials* **2023**, *16*, 924.
- [12] L. Zhang, Q.-Q. Zheng, S.-J. Xiao, J.-Q. Chen, W. Jiang, W.-R. Cui, G.-P. Yang, R.-P. Liang, J.-D. Qiu, *Chem. Eng. J.* **2021**, *426*, 131865.
- [13] a) S. Bolisetty, R. Mezzenga, *Nat. Nanotechnol.* **2016**, *11*, 365; b) M. Peydayesh, S. Bolisetty, T. Mohammadi, R. Mezzenga, *Langmuir* **2019**, *35*, 4161; c) M. Peydayesh, M. Pauchard, S. Bolisetty, F. Stellacci, R. Mezzenga, *Chem. Commun.* **2019**, *55*, 11143.
- [14] M. Peydayesh, R. Mezzenga, *Nat. Commun.* **2021**, *12*, 3248.
- [15] X. Ye, C. Lendel, M. Langton, R. T. Olsson, M. S. Hedenqvist, in *Industrial Applications of Nanomaterials*, (Eds: S. Thomas, Y. Grohens, Y. B. Pottathara), Elsevier, Amsterdam, the Netherlands **2019**, pp. 29–63
- [16] S. Ling, D. L. Kaplan, M. J. Buehler, *Nat. Rev. Mater.* **2018**, *3*, 18016.
- [17] T. P. J. Knowles, R. Mezzenga, *Adv. Mater.* **2016**, *28*, 6546.
- [18] a) G. Wei, Z. Su, N. P. Reynolds, P. Arosio, I. W. Hamley, E. Gazit, R. Mezzenga, *Chem. Soc. Rev.* **2017**, *46*, 4661; b) M. Peydayesh, M. Bagnani, R. Mezzenga, *ACS Sustainable Chem. Eng.* **2021**, *9*, 11916.
- [19] W. L. Soon, M. Peydayesh, T. de Wild, F. Donat, R. Saran, C. R. Müller, L. Gubler, R. Mezzenga, A. Miserez, *ACS Appl. Mater. Interfaces* **2023**, *15*, 47049.
- [20] M. Peydayesh, M. Bagnani, W. L. Soon, R. Mezzenga, *Chem. Rev.* **2023**, *123*, 2112.
- [21] Y. Cao, R. Mezzenga, *Adv. Colloid Interface Sci.* **2019**, *269*, 334.
- [22] M. Peydayesh, M. K. Suter, S. Bolisetty, S. Boulos, S. Handschin, L. Nyström, R. Mezzenga, *Adv. Mater.* **2020**, *32*, 1907932.
- [23] H. Motulsky, GraphPad Software, Inc., San Diego, CA **1996**.
- [24] M. D. Donohue, G. L. Aranovich, *Adv. Colloid Interface Sci.* **1998**, *76–77*, 137.
- [25] M. Peydayesh, A. Rahbar-Kelishami, *J. Ind. Eng. Chem.* **2015**, *21*, 1014.
- [26] K. Engelhardt, M. Lexis, G. Gochev, C. Konnerth, R. Miller, N. Willenbacher, W. Peukert, B. Braunschweig, *Langmuir* **2013**, *29*, 11646.
- [27] G. Nyström, M. P. Fernández-Ronco, S. Bolisetty, M. Mazzotti, R. Mezzenga, *Adv. Mater.* **2016**, *28*, 472.
- [28] a) C. Li, S. Bolisetty, R. Mezzenga, *Adv. Mater.* **2013**, *25*, 3694; b) S. Bolisetty, J. J. Vallooran, J. Adamcik, S. Handschin, F. Gramm, R. Mezzenga, *J. Colloid Interface Sci.* **2011**, *361*, 90.
- [29] L. Lv, X. Wu, Y. Yang, X. Han, R. Mezzenga, C. Li, *ACS Sustainable Chem. Eng.* **2018**, *6*, 12419.
- [30] L. Freitas de Freitas, G. H. C. Varca, J. G. Dos Santos Batista, A. Benévolo Lugão, *Nanomaterials* **2018**, *8*, 939.
- [31] S. Krishnamurthy, A. Esterle, N. C. Sharma, S. V. Sahi, *Nanoscale Res. Lett.* **2014**, *9*, 627.
- [32] J. Zhou, A. Saha, J. Adamcik, H. Hu, Q. Kong, C. Li, R. Mezzenga, *Adv. Mater.* **2015**, *27*, 1945.
- [33] N. Arena, J. Lee, R. Clift, *J. Cleaner Prod.* **2016**, *125*, 68.
- [34] Y. S. Ho, G. McKay, *Process Biochem.* **1999**, *34*, 451.
- [35] T. Walser, E. Demou, D. J. Lang, S. Hellweg, *Environ. Sci. Technol.* **2011**, *45*, 4570.
- [36] R. Arvidsson, D. Kushnir, B. A. Sandén, S. Molander, *Environ. Sci. Technol.* **2014**, *48*, 4529.